J Mater Sci (2022) 57:11918–11933

Metal Additive Manufacturing

Micro-scale thermodynamic model of microstructure and stress evolution in parts via selective laser melting

Ze-Chen Fang[1,2], Zhi-Lin Wu[1,*], Chen-Guang Huang[2], and Chen-Wu Wu[2,*]

[1] School of Mechanical Engineering, Nanjing University of Science and Technology, Nanjing 210094, China
[2] Institute of Mechanics, Chinese Academy of Sciences, Beijing 100190, China

Received: 13 October 2021
Accepted: 21 February 2022
Published online:
11 March 2022

ABSTRACT

The thermodynamic state changes during selective laser melting (SLM) processing dominate the microstructure and mechanical properties of the built parts. Improper operational parameters often lead to uneven microscopic morphology, microcracks, distortions, and other failures. The key to controlling the microstructure of the forming metal lies in an in-depth understanding of the micro-scale thermodynamics of this process. A micro-scale thermodynamic model was developed herein to predict the microstructure and internal stress evolution in parts fabricated by SLM with two typical scanning strategies. The modified two-temperature (TTM) model was employed to discover the dominant interface thermodynamic phenomenon in unitary path scanning and the novel symmetrical multi-path scanning capable of reliving residual stress and homogenizing microstructure. The real-time identifying method of temperature, microstructure, and stress could be further applied to closed-loop control of the SLM process.

Introduction

Selective laser melting (SLM) is one of the most widely used additive manufacturing forming technology for metal parts in decades [1–3]. Although this rapid prototyping technology has achieved pounds of progress in theory and practice with high machining precision, it is still facing the challenges of controlling the residual stress accumulated during layer-by-layer melting and solidification, which hinders its further application in cutting-edge and high-end fields [4–7]. The inadequate or excessive phase changes retained in the deposited layers after the SLM process induce uneven residual stress distribution and further unavoidable failures not selective to material, time, or location, such as common cracks and distortions, directly reducing the printing formability [8, 9]. This problem puzzles hot section components, large bridge structures, thin-walled

Handling Editor: M. Grant Norton.

Address correspondence to E-mail: wuruinan-1994@mail.njust.edu.cn; chenwuwu@imech.ac.cn

https://doi.org/10.1007/s10853-022-07046-6

overhanging parts, and other complex components particularly. The laser printing of SLM experiences thermodynamic processes in multiple time scales and space scales, such as microstructure evolutions after directly laser melting, molten pool behaviors in mesoscale, solid–liquid phase transition as path scanning, and additional re-melting during scanning of next layer. As a result, the defects can emerge in all space and time scales, for example, microcracks growth engendering the fatigue failure, brittle fracturing, and stress corrosion during the service period of the SLM-fabricated parts [10–12], which is responsible to lower high cycle fatigue strength even after hot isostatic pressing (HIP) than that in forging parts [1].

Our recent review [13] has systematically analyzed the methodologies to mitigate residual stress in numerical modeling, experimental characterization, parameter effects, pre-treatment, and post-treatment. Alleviating the high temperature gradient based on the critical temperature gradient mechanism (TGM) proposed by Mercelis and Kruth [5] is the current emphasis. A series of thermo-mechanical analytical models were developed which can roughly estimate the thermal stress distribution. Simulations and experiments related to TGM have achieved remarkable progress for certain materials as well, substantially relieving the distribution of residual stress and distortions. Unfortunately, lacking understanding of the microphysical mechanism, such trial-and-error solutions consuming a lot in computation resources and experimental versatility are not thorough and universal enough. The multi-scale characteristic of thermal–material–mechanical coupling in the SLM process makes it unrealistic to control residual stress only by a macro continuum mechanical model [14]. Considering that the unitary laser-powders interaction of SLM is within laser spot (in micro- and mesoscale), it is worthy to explore the relationship among the thermal field, microstructure, and force field on a smaller scale during metal powders rapidly evolving into solids, for eliminating the residual stress fundamentally.

Some enlightened attempts in mesoscale or microscale are emerging and developed rapidly in recent years. As a breakthrough to identifying individual powder sintering, the lattice Boltzmann method was introduced by Carolin Körner's team [15] and has evolved into a three-dimensional simulation framework covering multiple subprograms of physical fields from a simple two-dimensional model [16]. Established by kinds of software packages such as ALE3D, CFD-ACE +, and OpenFOAM, the mesoscale analysis models pay more attention to the laser–material interaction phenomena and mechanisms in molten pool size such as melt flow, spattering, and voids [17]. The microscopic modeling of the SLM process is considered in the initial stage. Powerful methods in microanalysis such as the Monte Carlo method and Molecular Dynamic method (MD) have been adopted to predict some thermo-mechanical characteristics of powder material. The Monte Carlo method has great advantages on uncertainty analysis during the energy transfer between energetic free electrons and material atoms [18–20]. It has been employed to simulate the grain growth during the multi-layer deposition of Inconel-718 to analyze the effects of melt flow rate and shape on the inhomogeneity microstructure of AM parts [21]. The MD calculation has also been implemented to acquire related thermal and flow properties needed in macro simulation [22]. Besides, an equivalent laser source model derived by microphysical mechanisms greatly improves the prediction accuracy of part distortion and residual stress in the macro model [23]. From a micro perspective, these attempts have found some unusual phenomena and in-depth laws that differ from the macro model but are slightly less systematic. The multi-scale modeling combined the advantages of the macro model (global fast predicting of part forming) and micro model (real-time local recognizing of physical mechanisms), which is promising for realizing the closed-up control of residual stress in the SLM process [24, 25]. Its maturity is also a key condition to realize the preparation of hierarchical structure and material-function integration by the SLM process [26–28].

Some studies have primarily investigated the effects of thermal parameters in micro-scale of the SLM process on the evolution of macro residual stress[29]. The direct thermo-mechanical coupling in micro-scale and basic micromechanisms of the SLM process is arduous and has breakthrough significance. Especially, the quantitative description of residual stress is truly needed. Fortunately, there have been articles emerging recently, focusing on the SLM process in the atomic scale and covering the study of parameter space, phase change, and microstructure evolution [30, 31]. Our group expects to establish a systematic multi-scale framework to

realize the precise control of residual stress of parts fabricated by SLM. The first thing to do is to develop the micro SLM model, which is the underlying core of the multi-scale framework. Therefore, we proposed a micro-scale model with a volumetric laser source to hunt the evolution law of microstructure and quantitatively identify the local temperature and stress fields.

Unitary scanning

Unitary scanning modeling

As mentioned above, an individual method like the finite element method (FEM) cannot describe the complex coupling of multi-physics fields in the SLM process precisely [13, 32]. Hence, we expect to further explore the micro-scale modeling of its basic thermodynamic process. The molecular dynamics method is the cornerstone of the micro-scale numerical model, which has been calculated by an excellent open-source software—large-scale atomic/molecular massively parallel simulator (LAMMPS). As shown in Fig. 1a, a hexagonal close-packed (HCP) titanium cluster model with a radius around 6A after the relaxation at 300 K for 500 ps was built firstly. As a template, it was deposited randomly on the substrate layer model in Fig. 1b forming a powder layer approximately 5 nm high. The simulation region contained a total of 104,844 atoms, which were examined in large batches to balance the convergence of the calculation engine and computation consumption. Periodic boundaries were set in both the X- and Y-directions with non-periodic, shrink-wrapped boundaries set in the Z-direction to prevent atoms from evaporating out of the simulation box during laser melting. The initial atom temperature is 300 K. The depth of the incident direction is far less than 10 nm, which does not satisfy the assumption of a surface source. Thus, we introduced a volumetric source as shown in Fig. 1(c) that has Gaussian distributing on laser radial plane and attenuating and aligns Lambert–beer law in the laser incident direction:

$$q = I_0(1-R)\exp\left\{-\frac{[x^2+y^2]}{\sigma^2}\right\}\exp\left(-\frac{L_Z-L_0}{L_0}\right), \qquad (1)$$

where I_0 is the input volumetric energy density and R is the laser reflectivity set to 0.55 for Ti.L_Z is the incident distance from upper cluster to deposited layer interface, and L_0 is the absorption distances which is set to 65A. The energy input is located in the midpoint of the top powder layer in Fig. 1b. Note that the unit of energy source derived from the energy balance partial differential equation is energy per unit time consisting of the units in LAMMPS for

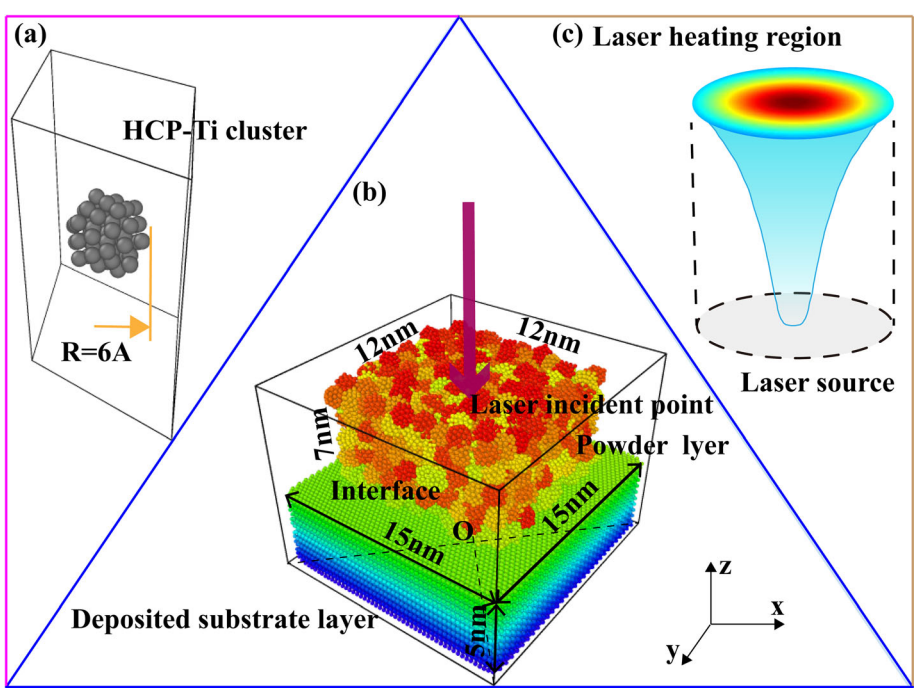

Figure 1 Framework of micro-scale model for selective laser melting in unitary single-point scanning.

mass, length, and time which is equivalent to 10 mJ/cm^2.

There are multiple time scales during laser interacting with metal powders, such as electron-to-electron energy diffusing to quasi thermal equilibrium with the Fermi Dirac law in hundreds of femtoseconds, electron-to-phonon energy relaxation less than 1 ps, and phonon energy transporting between metal lattice over tens of picoseconds. The two-temperature model (TTM) proposed by Kaganov et al. [33] is helpful to describe these energy couplings clearly. We successfully imported a modified TTM energy source to the MD system for unitary laser scanning by the Atom-to-Continuum package (AtC). In this extended TTM [34], the energy transport of the phonon system in the FE system is replaced by the atom system (energy changes between kinetic energy and potential energy) adhering to the law of energy conservation [34]. Through the node shape function, node temperature obtained by TTM achieved direct bidirectional coupling with atom kinetic energy.

Besides building the MD system of selective laser melting, a series of setups are needed for TTM coupling, such as specifying FEM fields, meshing the FE domains, assigning the related material file, initializing the thermal control method, and associating element tags with laser-affected areas. Because the MD region was fully overlapped the FE domains, there was no need to set an added fictitious boundary between the MD and the FE regions to control the thermal flux. The FE region of the laser has meshed to uniform elements as shown in Fig. 2. Consistent with the atomic temperature, the initial phonon and electron temperatures were both set to 300 K ensuring an equilibrium state for loading the three-dimensional Gaussian laser source. The laser–material interaction of the SLM process based on the extended TTM was activated by the dependent Verlet time-integration algorithm. The law of Gaussian least constraint, which is capable of describing both instantaneous and local propositions, was applied in the AtC package to construct the isokinetic thermostat which controls the interior thermal flux within the MD domain after electron energy relaxation.

Temperature fields in multi-time scales

The coupling process of laser energy and powder layer is mainly divided into three stages: electron-to-electron, electron-to-phonon, and phonon-to-phonon [34]. The first two stages involve two systems, so we employed the two-temperature model to simulate the direct energy transfer. The temperature fields of the TTM laser source coupling stages calculated by the AtC package are shown in Fig. 2. After about 2.5 fs (at the time A in Fig. 2b), the electron energy diffused radially and downward to a quasi-equilibrium state. Comparing Fig. 2a and Fig. 2b, the phonon temperature curve had the same trends but lower amplitude as electron temperature at the same node in the FE system derived by the two-temperature model. The phonon temperature gradually increases to balance with the electron temperature, completing the energy coupling of electron to phonon. It can also be observed from Fig. 2 that the amplitude of atomic temperature is close to that of node temperature, which proves the successfully coupling between the MD system and the FE system. Through shape function and energy conservation theorem, the atomic temperature matched with the node temperature in similar coordinates to replace the phonon energy diffusion in the MD system. The kinetic energy of clusters within laser spot increased rapidly, causing outer atoms to gradually dissolve and scatter into the interiors of neighboring powders.

Besides atomic temperature, the local temperature of the laser melting region in different heights is provided by Fig. 3 as well. The entire model was divided every 5A distance along the z-axis starting from the origin O in Fig. 1. Through grasping the propagation of local temperature histories in the multi-time scale, the second primary temperature gradient that rises upward from the interface to the top powder layer was found beside the radial temperature rising. As shown in Figs. 3a and b, it is worth noting that in the stages of electron-to-electron and electron-to-phonon energy diffusion, the region around 60A height experienced the highest average temperature among the overall simulation region. This phenomenon indicates that the interface between the bottom powder layer and deposited substrate layer absorbed more electron energy from the laser source, further reflecting partial energy to upper particles. Thus, a new path of heat flux formed beyond the initial radial propagation path of direct laser energy. Otherwise, the chaotic distribution of particle coordinates and the massive gaps between metal powders resulted in the oscillation of local average temperature which is more obvious than that in the deposited substrate layer.

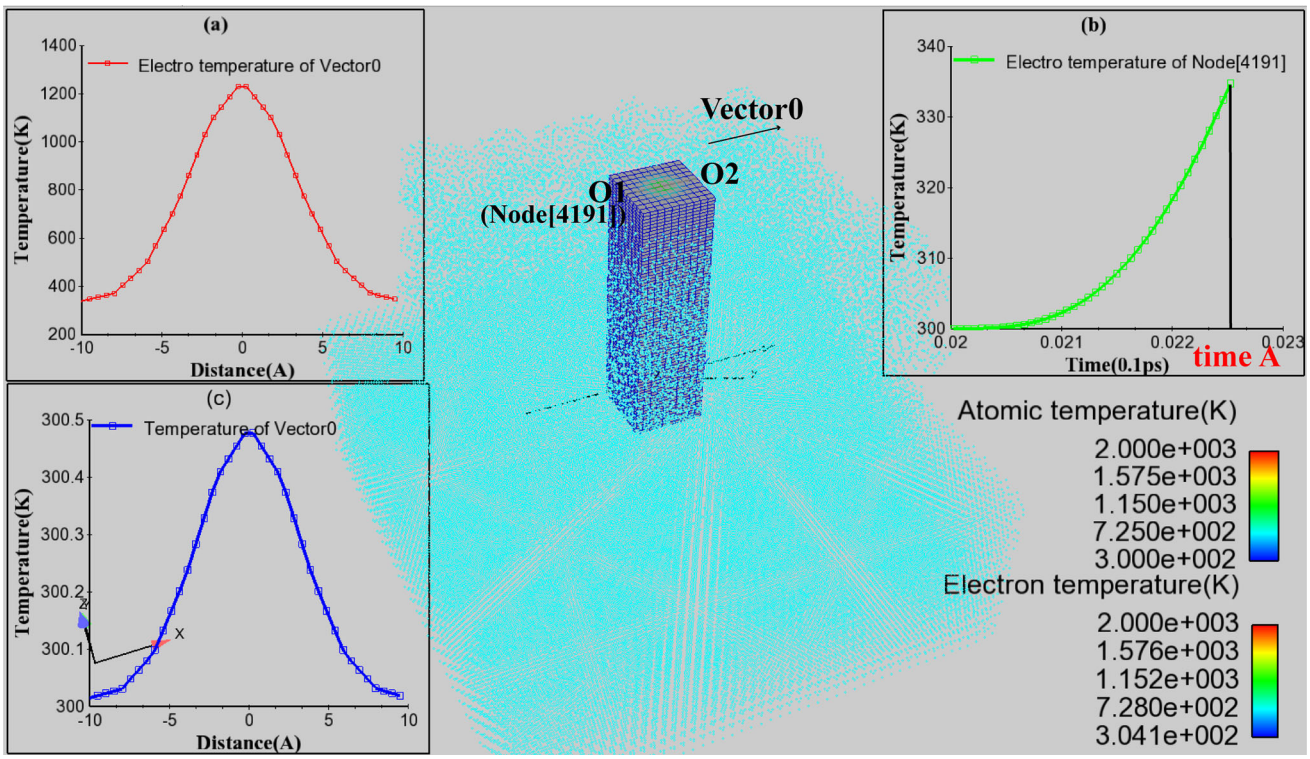

Figure 2 Radial temperature fields in electro-coupling scales: **a** the electro-temperature distribution along Vector0 (O_1O_2) at time A; **b** the time-varying electro-temperature cure of Nodel[4191] (location at point O1); (3) the electro-temperature distribution along Vector0 (O_1O_2) at time A.

It is summarized from Figs. 2 and 3 that induced by the two-temperature laser source, there are two primary paths of atomic heat transfer in the powder layer, which are along the laser radial direction and upward from the interface, respectively. The large top-to-bottom temperature gradient heralds the dominant position of the interfacial thermal path to the subsequent evolutions of phase transition and force field in the powder layer.

Microstructure evolution

Figure 4a shows that at first, the melting of the powder layer synchronously started from two regions that the central area near the laser direct heating region in Fig. 1(c) and the bottom near interface then expanded radially and upward. Affected by the direct energy coupling of electron-to-phonon laser heating as shown in Fig. 2, the central area of the cluster layer formed a significant radial temperature gradient, which leads to the expansion of melting along the radial direction. The other melting direction was consistent with the heat transfer path detected from Fig. 3, confirming that the interface has received massive electro-energy than the region at other heights and formed a bottom-up thermal reflection. Tracking back to the origin, this phenomenon can be explained by the difference in atom distribution between the cluster layer and deposited substrate layer. There are fewer direct energy contacting points between neighboring powders due to spherical shape than that in continuum deposited substrate layer, leading to a large number of internal cavities at the same time.

As the result of internal cavities of the powder layer, part of the incident laser energy can be directly transmitted to the interface, and benefiting from the leak-tight atomic arrangement, more atoms on the interface can be activated by the immediate laser energy than that on the powder layer within same spot range. Furthermore, the back-and-forth reflection of electron energy in the cavities consumed a lot, hindering its transport, whereas the conduction loss of electron energy between interface atoms is much less. Thus, the primary temperature gradient arises from the deposited layer interface resulting in melting direction from bottom to top of the powder layer.

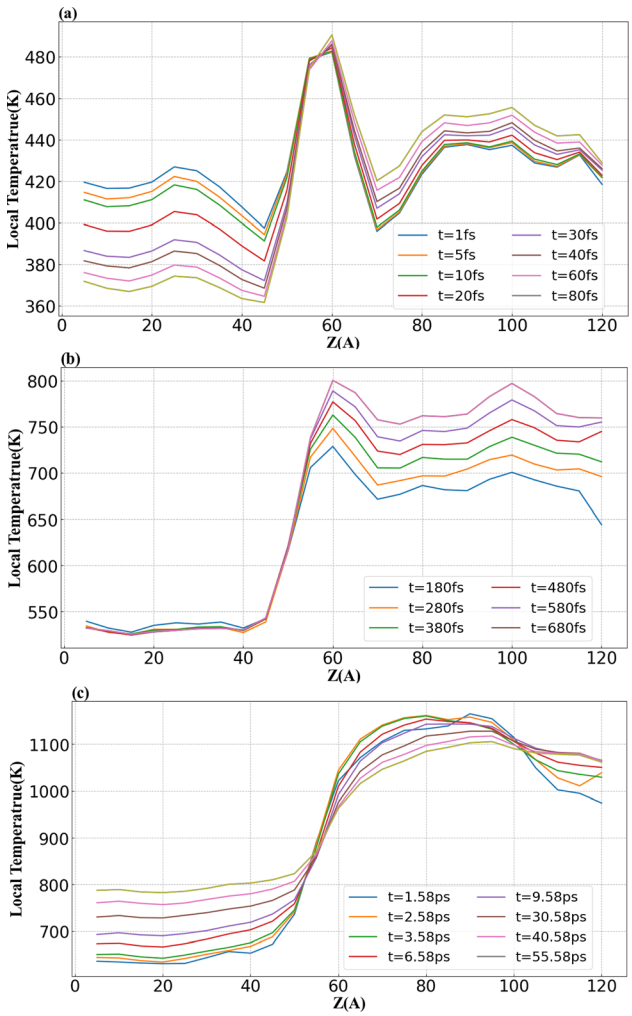

Figure 3 Local temperature fields of different heights: **a** electron-to-electron energy diffusion stage; **b** electron-to-lattice energy coupling stage; **c** lattice temperature relaxation stage.

The Ackland–Jones analysis was employed to characterize the evolution of phase change which is shown in Fig. 4b. A distinct phenomenon is observed that the melted cluster layer solidified layer-by-layer into an HCP lattice structure from bottom to top. The decreasing of temperature gradient as the heat of molten cluster layer transporting to the deposited substrate layer is responsible for this phenomenon. Both melting and solidification processes all proved that interfacial energy transfer dominates the entire thermodynamic change of unitary scanning of the SLM process. The interface atoms of the deposited substrate layer firstly absorbed a large amount of electron energy from the laser source and then transmitted them to both sides, driving the bottom-to-up melting and solidification direction of the clusters.

Residual stress identifying

The 6-element stress tensor per atom in the MD system calculated by LAMMPS is shown in formula (2) as follows:

$$S_{ab} = -mv_a v_b - W_{ab}, a, b \in (x, y, z), \tag{2}$$

where a, b denote the specific stress component (for example, σ_{xx} is the diagonal components in the x-axis). $-mv_a v_b$ is a kinetic energy-related term. The other term $-W_{ab}$ is derived by the Viral theorem representing intra- and inter-molecular interaction in the entire system. The computation of the Viral contribution has been described in detail in the literature [35]. For delineating the atomic stress, we imported a concept similar to hydrostatic pressure, using the average of principal stress to estimate the magnitude of the atomic stress. Note that the stress tensor directly computed by LAMMPS is a "pressure × volume" quantity.

Calculating the volume for an individual atom is difficult, especially for metal forming. Although there are methods such as the Voronoi method to roughly estimate atomic volume during the simulation process, it introduces new errors and is unnecessary. Therefore, we first measured the severity of the residual stress using the atomic stress in LAMMPS's unit ("Bar·A^3" for "metal unit") without divided by atom volume as shown in Fig. 5, and then selected a reasonable method to divide the model for calculating the local stress in formula (3) [36]:

$$\sigma_{vol} = \sum_{i=xx,yy,zz} \sigma_i/(3 \cdot vol), \tag{3}$$

where σ_{vol} denotes the local stress, σ_i is the principal stress tensor, and vol represents the local volume for the selected titanium region. By formula (3), the distribution of local residual stress having macroscopic meaning was obtained.

After undergoing melting, the cluster layer began to solidify with the liquid phase transforming into the HCP phase similar to the deposited layer, which is obvious in the partially enlarged image shown in Fig. 5(d). As shown in Figs. 5a-(c), the inhomogeneity of the cluster layer microstructure becomes more and more severe from the interface to the top cluster, which exacerbates the residual stress in the upper

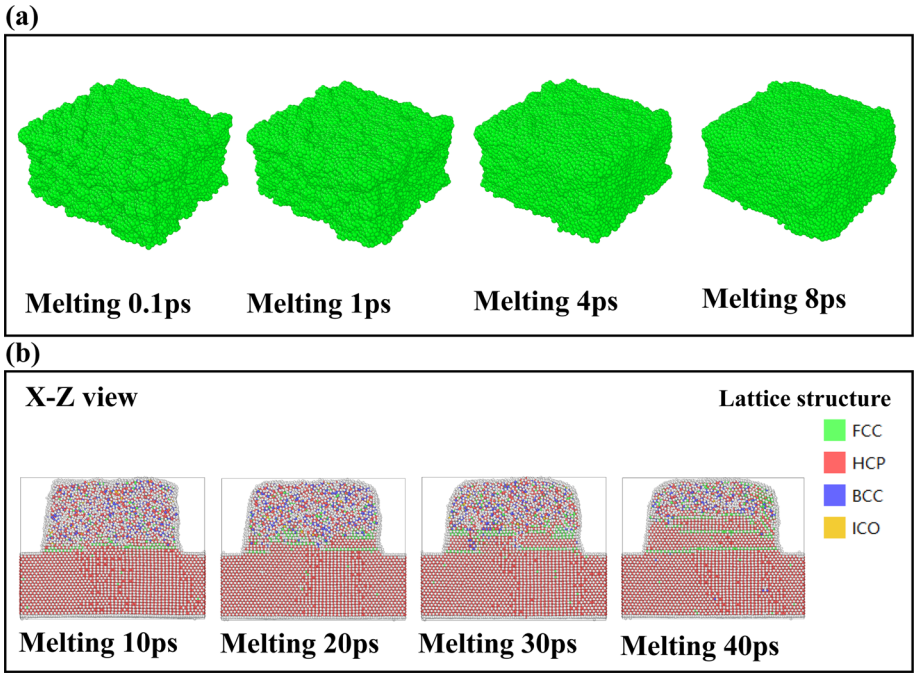

Figure 4 Phase state and microstructure evolution of titanium cluster powder.

region and forms an evident boundary above the regular HCP structure in the enlarged view of Fig. 5(c). Even though the temperature rise is insufficient to cause large-scale phase changes, it still lead to sporadic dislocation and unbalanced local stress in the deposited substrate layer (see Fig. 5b). It was also observed that the HCP grain boundary is consistent with the atomic stress contour from Fig. 5(c).

The local volume can be selected as required for specific geometry when calculating local stress. Here, we take the midpoint of the interface as the center, and every 10A, take the hemispherical ring in the powder layer and the deposited layer as the local volume statistical range as is shown in Fig. 6. Firstly, during the cooling and solidifying of the bottom cluster layer, the internal tensile stress was generated because of the confinement of the underlying deposited layer. Then, as the solidification spreads upward, each new solidified layer is subjected to tensile stress from below the powder layer. Accordingly, part of the stress in the previously solidified phases will be transformed into compressive stress to balance the tensile stress above it. Looping as the above manner, staggered distribution of tensile stress and compressive stress in the solidified powder layer was formed effected by asynchronous solidification and shrinkage, which is consistent with the local stress distance–varying curve and distribution contour of powder layer in Fig. 6. However, the heat transfer is unidirectional in the deposited layer. Therefore, this region experiences pure thermal expansion that induced uniform tensile stress. The overall stress level in the deposited layer is lower than that in the granular layer as the curves in Fig. 6 show. Due to the heat reflection and heat conduction effects of the interface, the surrounding particles became the earliest area that experienced melting and solidification, making it become the most synchronous thermodynamics area. The powder layer above the interface which is in uniform microstructure after full phase change has a lower residual stress level than that in the top layer with chaotic texture.

In summary, decided by the asymmetry of the laser energy loading, the inconsistency between heat flux and dissipation conditions throughout the cluster layer resulted in asynchrony phase change and staggered residual stress. The local stress in the interface has been balanced by the powder layers below and above. In addition, the center of the interface has a sharp rise of residual stress that may be affected by the intense reduction of local volume. The heterogeneous microscopic stress distribution has a close relationship with the asymmetric multipath heat transfer of instantaneous high electron energy. As and result, the laser radiation and cooling times are crucial to the final state. Insufficient cooling time exacerbates the residual stress accumulation.

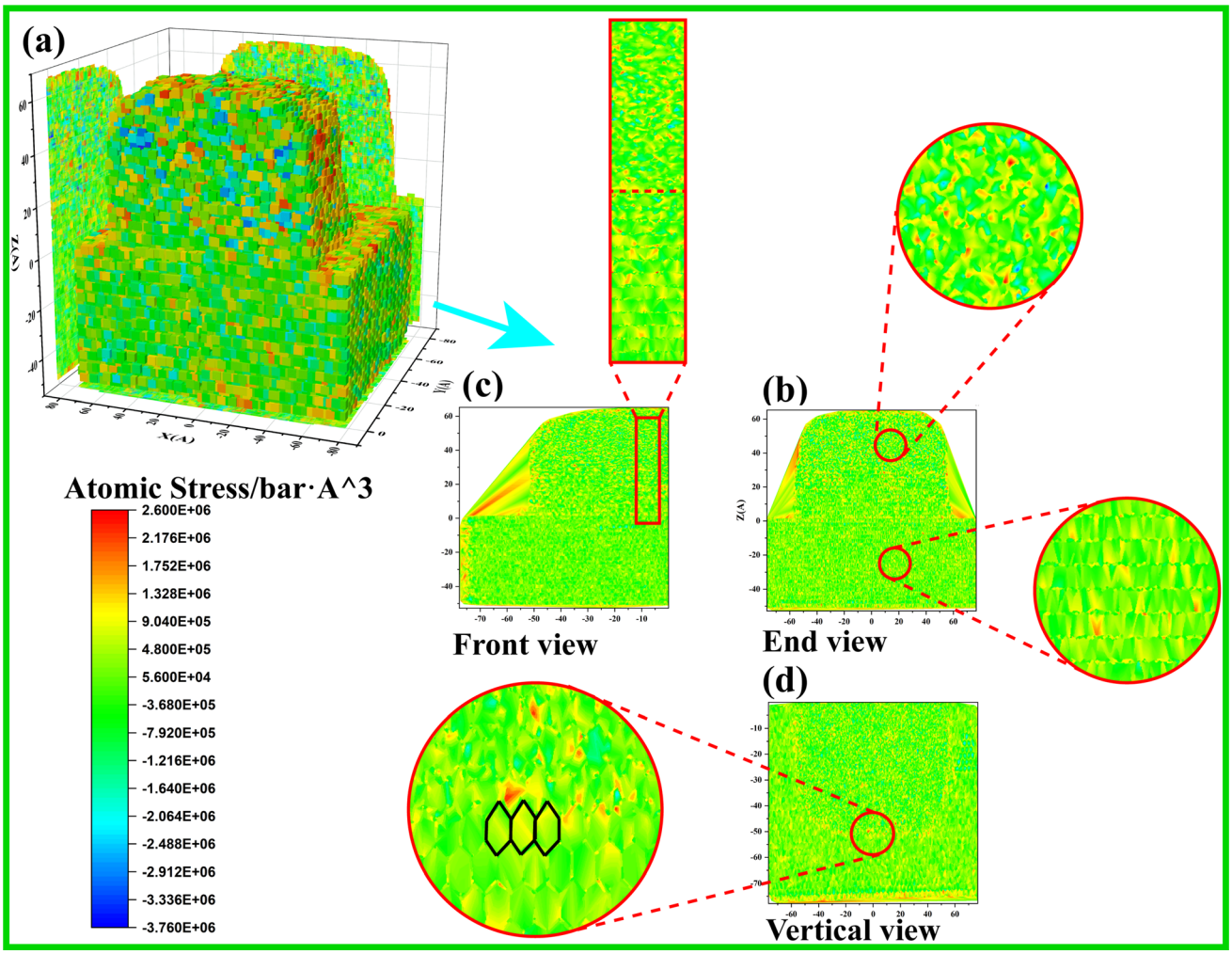

Figure 5 Atomic stress distribution for the solidified cluster layer at 55 ps: **a** the three-dimensional distribution; **b**–**d** the atomic stress of main views and their local amplification.

More seriously, the reinforcement effect of high processing speed further hinders the formation of a uniform and free-residual stress microstructure. From this perspective, the residual stress can be effectively reduced through the auxiliary measures of stress releasing or the implemented processing that alter asymmetric heat transfer to fulfill complete and uneven phase change.

Electron-atom energy coupling mechanism

The stress states of the cluster and deposited layers after solidification have a close relationship with the heat transfer mechanism of selective laser melting. Through the above analysis of temperature field, phase change, and stress distribution, we draw the electro-energy evolution in Fig. 7.

Inspired by these microscopic physical phenomena, we proposed the following theoretical model combined by the traditional two-temperature model with the unique interface and interior thermodynamics mechanism:

$$\begin{aligned} \rho_{ce} c_{ce} \dot{\theta}_{ce} &= -\nabla \cdot q_{ce} - g_c + \rho_{ce} r_{ie} + n \cdot q_{re} \\ \rho_{cp} c_{cp} \dot{\theta}_{cp} &= -\nabla \cdot q_{cp} + g_c + \rho_{cp} r_{ip} \end{aligned}, \quad (4)$$

where ρ_{ce} and ρ_{cp} are the respective equivalent mass densities of the electro- and phono-systems in the cluster layer which are equal to the total atomic masses divided by the particle layer volumes, c is the heat capacity coefficient for the temperature field θ of the electro- and phono-systems, respectively, q_{ce} and

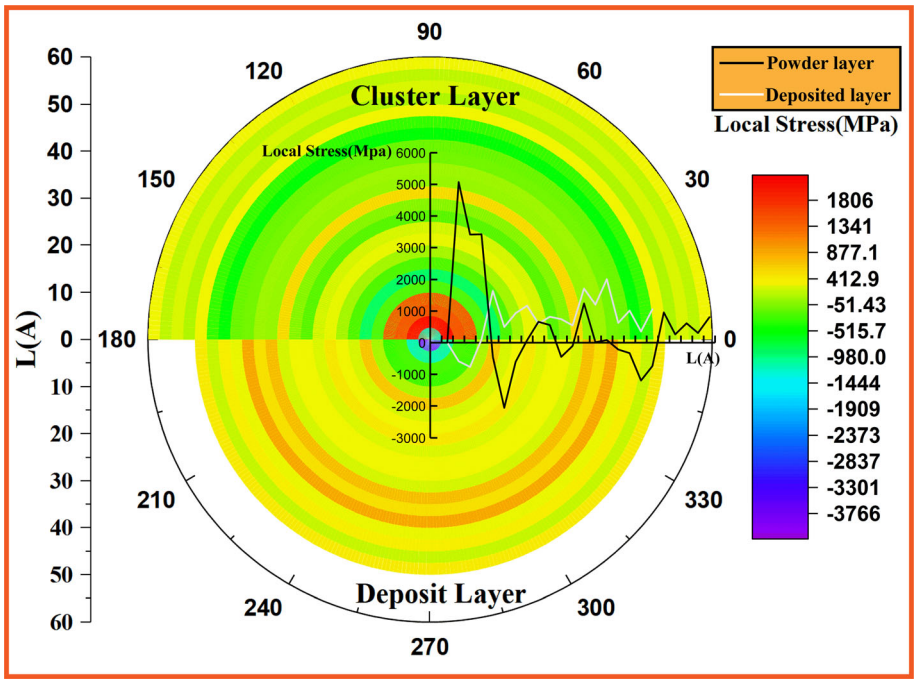

Figure 6 Quantitative identification of local residual stress in hemispherical ring regions every 10A radius.

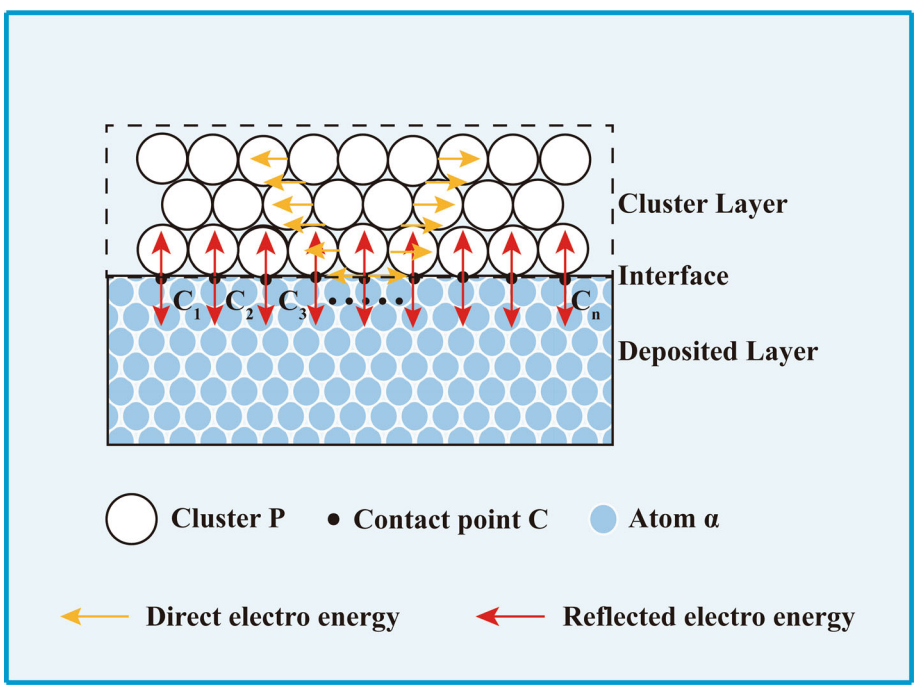

Figure 7 Electron-to-atom energy coupling model of selective laser melting in micro-scale.

q_{cp} are the heat fluxes transported in the respective systems, g is the well-known electro-phono coupling rate, $\rho_{ce}r_{ie}$ and $\rho_{cp}r_{ip}$ are the operators for the external source (immediate electro-energy), and n is the outward unit normal vector. The terms $n \cdot q_{re}$ and $n \cdot q_{rp}$ are destitute in the original TTM and represent the interface fluxes generated by the reflected electro- and phono-energies, respectively. The heat fluxes q_{ce} and q_{cp} are derived from the Boltzmann transport equation and have the following typical form corresponding to diffusive Fourier behavior:

$$q_{ce} = -k_{ce}\nabla\theta_p, \tag{5}$$

where k_{ce} is the conductivity tensor which is consant for isotropic material and has been extended to

satisfy pure disorderly stacked powder flows according to [37] as follows:

$$k_{ce} = k_{ce0}\theta_p^{1/2} I, \tag{6}$$

where the modified k_{ce} is proportional to the square root of the local average temperature of the clusters via k_{ce0} (a conductivity coefficient determined by the material, cluster geometry, and arrangements of the clusters). Increasing the number of small particles and/or clustering them closer to each other increases k_{ce0}. As the structure of the particle layer approaches homogenous isotropic material, $k_{ce0}\theta_p^{1/2}$ approaches the heat conduction constant. Because the heat conduction efficiency of electron and phonon energy in the granular layer is much lower than that in the homogeneous continuous deposited layer, the time needed for electron energy diffusion from the interface spot area to the entire interface (less than 0.1 ps) can be ignored. Hence, the diffusion of the interface electron energy from the contact point to the cluster layer is introduced into the two-temperature model as a heat flux reflected by the interface. In fact, the presence of particle voids causes energy that should have been deposited on the cluster layer reaches to the interface, forming an enhanced energy gradient at the interface that accelerates the temperature rise and melting of the underlying particles. The energy deposited at the interface can be obtained from the laser surface energy density as follows:

$$\int_{\partial\Omega_i} n \cdot q_{re} = R_d \int_{\partial\Omega_l} n \cdot q_{ie}, \tag{7}$$

where Ω_i is the complete integral domain of the interface, Ω_l is the laser spot integral domain of the interface, q_{ie} is the laser energy density that directly interacts at the interface, and R_d is the reflection ratio of the homogeneous deposited layer material.

Reference [38] provided temperature gradients at different depths of the macro SLM process. Under the action of the similar volume Gaussian heat source, along the incident direction of the laser, the magnitude of the temperature gradient (G) first increases to a maximum value and then begins to decrease. The maximum magnitude of G appears near the powder–solid interface. Since there is no other heat source term in the energy equation, this also confirms that the heat in this system increases originating from the boundary condition of the interface. We further normalized the temperature gradient and depth of this article and reference [38]. Calibrating the interface as zero to normalize the depth, the distance above the interface is positive, and vice versa. The normalized temperature gradient is named G′. As shown in Fig. 8, the trend of the two temperature gradients shows a high degree of concordance, which proves that the heat transfer path reflected the interface between powder layer and deposited substrate layer is true and consistent in micro- and macro-scales. Due to the different source loading, the slope of the two temperature histories is slightly different.

Multi-path scanning

Multi-path scanning modeling

In "Unitary scanning" section, we have developed a unitary scanning model of the SLM process and obtained a unique interfacial thermodynamic mechanism. To probe more microscopic mechanisms, the model has been further extended to multi-path and multi-layer scanning of SLM. Meanwhile, the composition of the powder is also upgraded to a ternary alloy—Ti6Al4V for more practical purposes. The main architecture of the extensive modeling is shown in Fig. 9, which can be divided into two main cores: the control method for the multi-path printing and the layer-by-layer evolving process. For this multi-layer print, we has chosen a cylinder geometry with a radius of 54A and a height of 65A as the print object. After trial and error, it was found that using a "four-

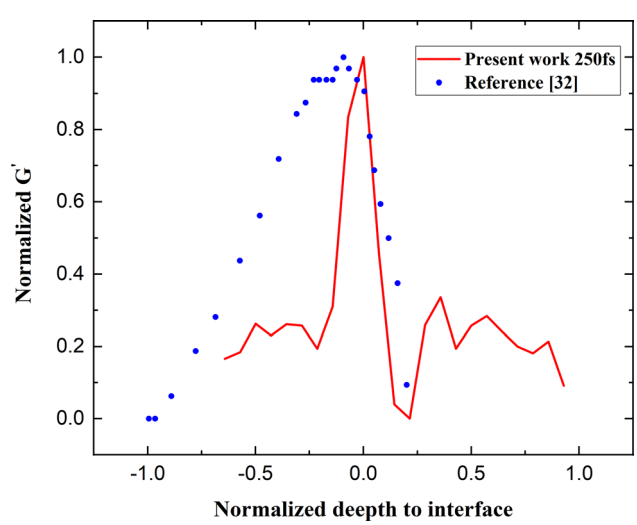

Figure 8 Normalized temperature gradient distribution in 250 fs in comparison to reference [32].

leaf clover mode" shown in Fig. 9a as a multi-circle scanning path had better filling effects for per cylindrical layer and was much easier to fulfill parametric control for spot moving. The spot coordinate parameters in "four-leaf clover mode" for layer N is described in formula (8):

$$\begin{cases} r = \dfrac{R}{2N} \\ r_N = (3N-1)r \\ \alpha = 2\arcsin\theta\sin\dfrac{(r-l/2)}{r_N}, \\ M = \mathrm{round}(\dfrac{\pi}{\alpha}) \end{cases} \tag{8}$$

where R is the radius of the entire layer, r is the radius of the laser spot, r_N is the coordinate of initial spot specified as (r_N, 0) of each layer, α is the offset angle for next spot, l is the hatch distance, and M is the numbers of laser spot for layer N. The print direction is counterclockwise along a circular path. The first key parameter is radius of laser spot r, which is decided by the layer radius R and the number of scanning turns N, which was around 9A for three cycle path printing in this simulation. The second key parameter of laser scanning control, the hatch distance l, determines the rotation angle α for the next laser print point along the circular path. We defaulted the first scanning circular path to be four mutually perpendicular light spots, thus determining the hatch distance per scanning. It is feasible to increase or decrease the number of scan points for a certain single circle to change the hatch distance for customized requirements. The center of the laser spot moves according to the scanning speed along the scanning circle. In this simulation, the scanning speed is 2.54 m/s, that is, 5000-time steps (0.001 ps) for individual scanning. Because there are too many times of laser scanning, it is computationally expensive to adapt to the TTM-based two-temperature model energy source. In this simulation of multi-path scanning, we simplify the light source to a cylindrical uniform light source. The energy densities of the laser source for the first layer, the second layer, and the third layer are 50 eV/ps, 80 eV/ps, and 100 eV/ps respectively, which are equivalent to 6.5 J/mm^3, 10.4 J/mm^3, and 13 J/mm^3.

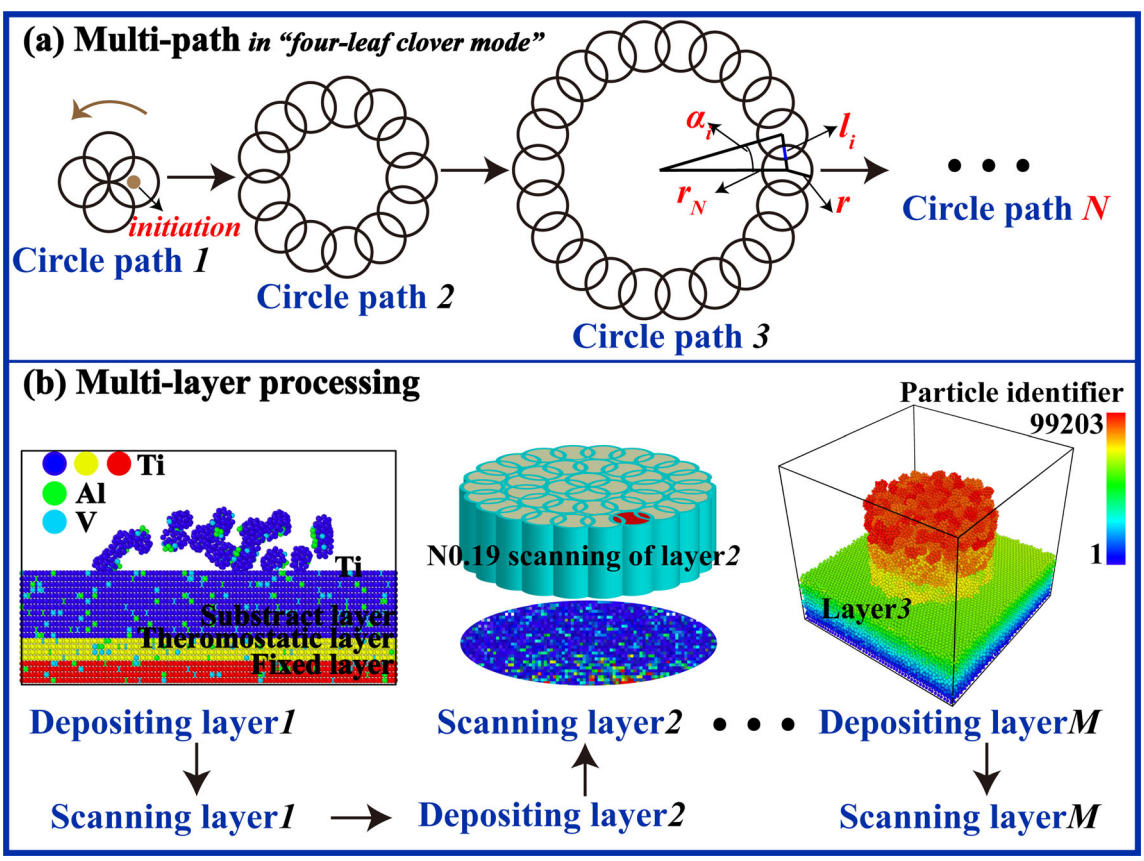

Figure 9 Modeling of multi-path and multi-layer scanning.

As shown in Fig. 9b, multi-layer printing is a progressive process. After a layer has undergone the melting and solidification process, powder deposition of this completed layer is needed to perform a new multi-path laser scan. The cylindrical part in this study was built by three layers of printing each of them with three circular tracks, with a total of 117 individual scanning points. Inspired by molecular dynamics simulations of nanoindentation, the second feature except for the "four-leaf clover mode" scanning for this extended model is dividing the deposited substrate layer into three layers which from top to bottom are the heat transfer layer (transferring energy from the upper powder layer), the thermostatic layer (withstanding a Langevin thermostat of 300 K to construct a boundary condition similar to room temperature), and the fixed layer (preventing the bottom atoms escaping from the box boundary), respectively. Consistent with the unitary model in "Unitary scanning" section, the powder spreading process was realized by the "fix deposit command" in LAMMPS.

Microscopic characterization

We identified the microstructure of the built workpiece by Ackland–Jones analysis in Fig. 10. After the printing of each layer finished, the powder layer would experience relaxation cooling for more than 1000 ps to form a stable structure at room temperature. As shown in Fig. 10b, the crystalline phase on the cross-section has an obvious feature: The lamellar sheet HCP α phase is staggered in the radial direction and tangent direction of circle scanning path, which differs from the well-known parallel staggered distribution of lamellar α phase of Ti6Al4V fabricated by linear scanning in Fig. 10a. This unique orientation is related to the "four-leaf clover mode" scanning introduced in "Multi-path scanning modeling" section. As the longitudinal microstructure section shows in Fig. 10(c), there is no obvious grain boundary between each layer, and the structure is relatively uniform, indicating that during the particles melting, the interface of the lower layer also remelted to a certain extent, forming an integrated structure.

3D stress quantification

To quantify the interior residual stress clearly, the cylindrical workpiece was divided every 10A along the z-axis direction. Taking its axis as the center, every local cylinder was divided every 10A radial distance, thus forming a three-dimensional local stress distribution contour as Fig. 11a shows. The calculation of the local stress is counted on formula (3). On the whole, the local stress level was in a decreasing trend from top to bottom. In every cylindrical region, the local stresses of the central region, the three middle regions, and the outermost region were in a staggered distribution of tensile stress–compressive stress–tensile stress. The compressive stress of the three middle regions decreases along the radial direction, and the central region was similar to the outer. The stress within the individual powder layer was relatively uniform, while the stress between the two powder layers had a clear boundary. Consistent with the conclusions in "Residual stress identifying" section, the residual stress in the region near the bottom was relieved as printing progresses, on the contrary, the stress in the outermost layer was significant that should be taken seriously. Compared to a unidirectional scan path, the "four-leaf clover mode" has natural symmetry which contributes to the self-balancing of residual stress within each powder layer.

To further characterize the failure surface of the printed part, the stress tensor derived from LAMMPS was employed to calculate the atomic-level stress triaxiality distribution on the stepped section as is shown in Fig. 10b. From the overall distribution of stress triaxiality, atoms with opposite stress states are alternately distributed, which has the effect of offsetting the residual stress. The large stress triaxiality value appeared near the interface of the powder layer which is easy to cause stress concentration, while the small stress triaxiality value generally occurred inside the powder layer which is prone to cause tiny voids inside.

As an emerging field, the mechanism of metal particles melting in micro-scale has attracted many researchers. A series of two-particle melting molecular dynamic models of nickel [39], iron [40], copper [41], and silver [42] have been performed using the Nose–Hoover thermostat by Jing Zhang's team. The average temperature history curves of whole systems can be derived along with the diffusion patterns of

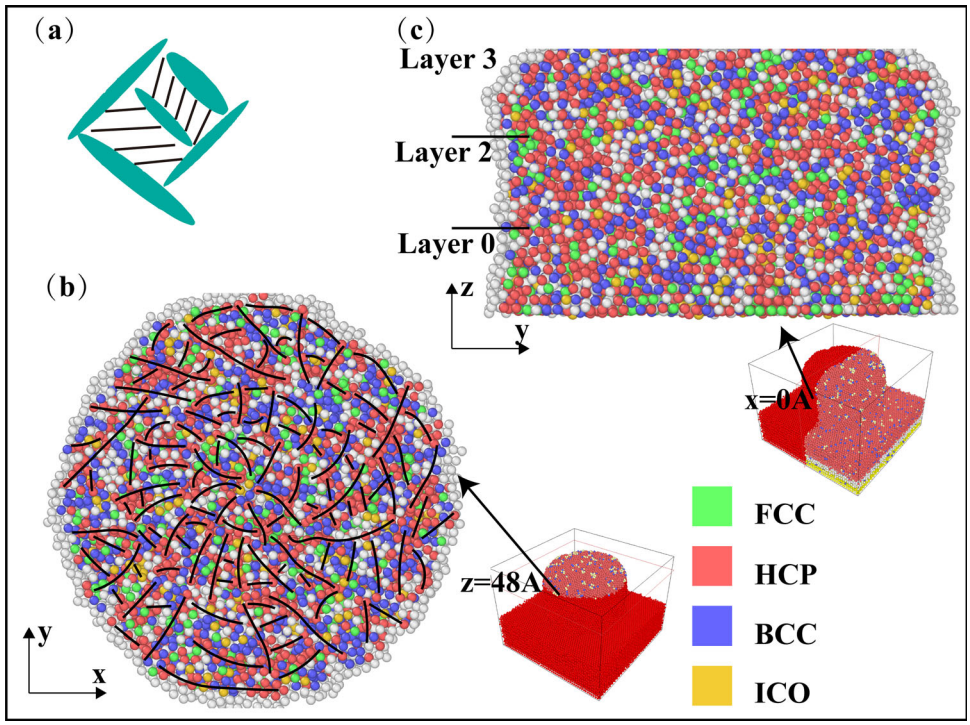

Figure 10 Microstructure characteristic in the longitudinal and transverse section at the height 48A.

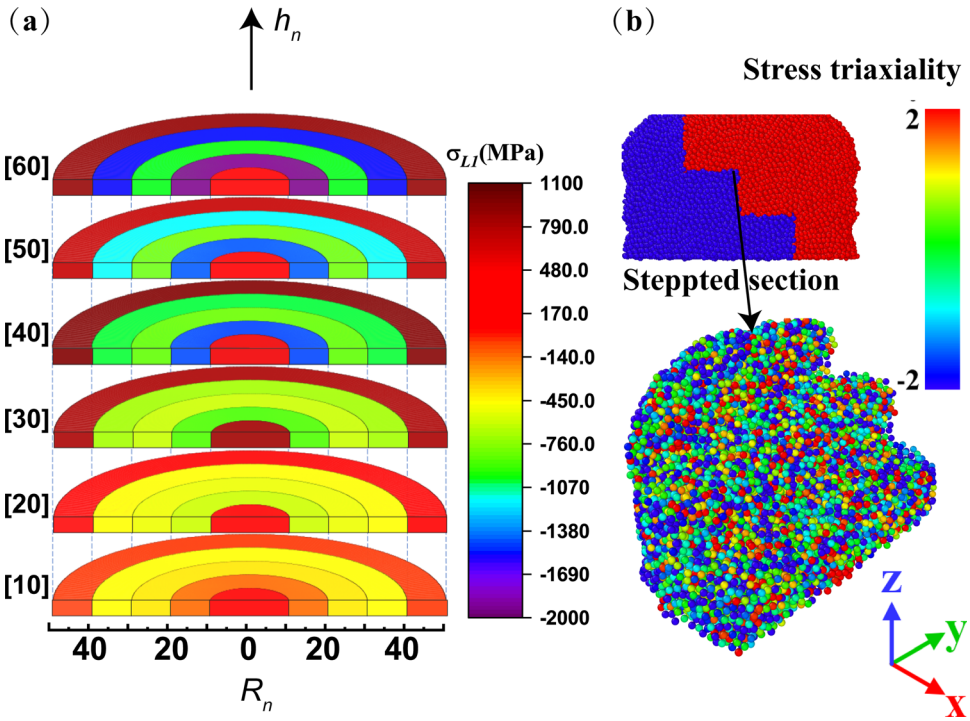

Figure 11 3D local residual stress of multi-layer scanning and stress triaxiality for stepped section.

two heated particles. In principle, these processes were quasi-static isothermal heating in which the temperature rise of the system increases linearly with time not being a transient laser plume. These models concluded that diffusivities were linearly related to temperature and the external energy mainly contributed to driving the local phase change surrounding atoms, suggesting that microscopic analysis is a powerful tool for discovering the direct relationship of phase change, mechanical properties, microscopic morphology, and thermal history between particles. A series of recent studies

employed the particles in a regular distribution to study the microscopic melting process of Cu50Zr50 alloy and other metals [30, 33, 43]. However, the two-particle system or powder layer in the regular arrangement cannot truly reflect the characteristics of the SLM material and the energy transfer interior the layers hardly provide a precise basis for further shape control. Different from the above research, the loading of external heat source in this paper was based on a transient mechanism, and the particle arrangement in a free and random distribution form to simulate the real environment of the powder layer. The model also considered the interaction between the melted particles, the interface, and the substrate. For further exploring the microscopic mechanism of the complete printing process of selective laser melting, we further imported a "four-leaf clover mode" for multi-path laser scanning with multi-layer simulation similar to the actual process, which is positive to build the subsequent multi-scale framework of the SLM process.

Conclusions

An atomic-scale unitary scanning model of SLM process coupling with TTM source was proposed at first to identify the thermodynamic evolution mechanism. Through quantitatively identifying atomic and local temperature, stress, and characterizing microstructure features, it was found that the interface reflection effect of laser energy is the origin of energy transferring from bottom to top and dissipating from top to bottom in the powder layer. The asymmetry of heat paths resulted in uneven phase change and heterogeneous stress distribution. The fluctuation of energy of powder layers close to the interface was more synchronized than other regions leading to uniform microstructure and lower local residual stress level.

Next, we extended the model to adapt the multi-path and multi-layer printing mode. A novel multi-circle scanning mode named "four-leaf clover mode" with flexible parametric controllability is proposed. Through the identification of the microstructure, it is found that the lamellar sheet HCP α phase of the Ti6Al4V built workpiece staggered along the radial and tangential directions of circle paths. The quantitative analysis of local residual stress indicates that the natural symmetry of the "four-leaf clover mode" is conducive to relieving stress.

Thermodynamic characteristics seriously affect the microstructure and distribution of residual stress, which are the key to designing parts with low residual stress levels and crack-free microstructures. The above models were capable of quantitatively describing the atomic and local physical quantities and internal transfer mechanism in real-time, which is helpful to realize the closed-up control of the SLM process.

Acknowledgements

This work was supported by the National Natural Science Foundation of China (Grant No. 11572327), the Strategic Priority Research Program of Chinese Academy of Sciences (Grant Nos. XDA17030100 & XDA17030200), and the Postgraduate Research & Practice Innovation Program of Jiangsu Province (Grant No. KYCX19_0273).

Declarations

Conflict of interest The authors declare that they have no known competing financial interests or personal relationships that could have appeared to influence the work reported in this paper.

References

[1] Arcella FG, Froes FH (2000) Producing titanium aerospace components from powder using laser forming. JOM 52(5):28–30. https://doi.org/10.1007/s11837-000-0028-x

[2] Yap CY, Chua CK, Dong ZL, Liu ZH, Zhang DQ, Loh LE, Sing SL (2015) Review of selective laser melting: materials and applications. Appl Phys Rev 2(4):041101. https://doi.org/10.1063/1.4935926

[3] Mines R (2019) Additive manufacturing processes and materials for metallic microlattice structures using selective laser melting, electron beam melting and binder jetting. Metallic microlattice structures, Springerbriefs in applied sciences and technology. Springer, Berlin, pp 17–31

[4] Koric S, Thomas BG (2008) Thermo-mechanical models of steel solidification based on two elastic visco-plastic constitutive laws. J Mater Process Technol 197(1–3):408–418. https://doi.org/10.1016/j.jmatprotec.2007.06.060

[5] Mercelis P, Kruth JP (2006) Residual stresses in selective laser sintering and selective laser melting. Rapid Prototyping

J 12(5):254–265. https://doi.org/10.1108/13552540610707013

[6] Gusarov AV, Pavlov M, Smurov I (2011) Residual stresses at laser surface remelting and additive manufacturing. Lasers in manufacturing 2011: proceedings of the sixth international Wlt conference on lasers in manufacturing 12(1):248–254. https://doi.org/10.1016/j.phpro.2011.03.032

[7] Huang J, Li M, Wang J, Pei Z, McLntyre P, Ma C (2021) Selective laser melting of tungsten: effects of hatch distance and point distance on pore formation. J Manuf Process 61:296–302. https://doi.org/10.1016/j.jmapro.2020.11.034

[8] Lu YJ, Wu SQ, Gan YL, Huang TT, Yang CG, Lin JJ, Lin JX (2015) Study on the microstructure, mechanical property and residual stress of SLM Inconel-718 alloy manufactured by differing island scanning strategy. Opt Laser Technol 75:197–206. https://doi.org/10.1016/j.optlastec.2015.07.009

[9] Parry L, Ashcroft IA, Wildman RD (2016) Understanding the effect of laser scan strategy on residual stress in selective laser melting through thermo-mechanical simulation. Addit Manuf 12:1–15. https://doi.org/10.1016/j.addma.2016.05.014

[10] Syed AK, Ahmad B, Guo H, Machry T, Eatock D, Meyer J, Fitzpatrick ME, Zhang X (2019) An experimental study of residual stress and direction-dependence of fatigue crack growth behaviour in as-built and stress-relieved selective-laser-melted Ti6Al4V. Mater Sci Eng A 755:246–257. https://doi.org/10.1016/j.msea.2019.04.023

[11] Eto S, Miura Y, Tani J, Fujii T (2014) Effect of residual stress induced by pulsed-laser irradiation on initiation of chloride stress corrosion cracking in stainless steel. Mater Sci Eng A 590:433–439. https://doi.org/10.1016/j.msea.2013.10.066

[12] Harrison NJ, Todd I, Mumtaz K (2015) Reduction of micro-cracking in nickel superalloys processed by Selective Laser Melting: a fundamental alloy design approach. Acta Mater 94:59–68. https://doi.org/10.1016/j.actamat.2015.04.035

[13] Fang ZC, Wu ZL, Huang CG, Wu CW (2020) Review on residual stress in selective laser melting additive manufacturing of alloy parts. Opt Laser Technol. https://doi.org/10.1016/j.optlastec.2020.106283

[14] De A, DebRoy T (2013) A perspective on residual stresses in welding. Sci Technol Weld Join 16(3):204–208. https://doi.org/10.1179/136217111x12978476537783

[15] Korner C, Attar E, Heinl P (2011) Mesoscopic simulation of selective beam melting processes. J Mater Process Technol 211(6):978–987. https://doi.org/10.1016/j.jmatprotec.2010.12.016

[16] Ammer R, Markl M, Ljungblad U, Korner C, Rude U (2014) Simulating fast electron beam melting with a parallel thermal free surface lattice Boltzmann method. Comput Math Appl 67(2):318–330. https://doi.org/10.1016/j.camwa.2013.10.001

[17] Qiu CL, Panwisawas C, Ward M, Basoalto HC, Brooks JW, Attallah MM (2015) On the role of melt flow into the surface structure and porosity development during selective laser melting. Acta Mater 96:72–79. https://doi.org/10.1016/j.actamat.2015.06.004

[18] Yan WT, Smith J, Ge WJ, Lin F, Liu WK (2015) Multiscale modeling of electron beam and substrate interaction: a new heat source model. Comput Mech 56(2):265–276. https://doi.org/10.1007/s00466-015-1170-1

[19] Zhang Y, Xiao XH, Zhang J (2019) Kinetic Monte Carlo simulation of sintering behavior of additively manufactured stainless steel powder particles using reconstructed microstructures from synchrotron X-ray microtomography. Results Phys. https://doi.org/10.1016/j.rinp.2019.102336

[20] Mohanty S, Hattel JH (2014) Numerical model based reliability estimation of selective laser melting process. In: 8th international conference on laser assisted net shape engineering (Lane 2014) 56:379–389. https://doi.org/10.1016/j.phpro.2014.08.135

[21] Wei HL, Knapp GL, Mukherjee T, DebRoy T (2019) Three-dimensional grain growth during multi-layer printing of a nickel-based alloy Inconel 718. Addit Manuf 25:448–459. https://doi.org/10.1016/j.addma.2018.11.028

[22] Zhang J, Zhang Y, Lee WH, Wu L, Choi H-H, Jung Y-G (2018) A multi-scale multi-physics modeling framework of laser powder bed fusion additive manufacturing process. Met Powder Rep 73(3):151–157. https://doi.org/10.1016/j.mprp.2018.01.003

[23] Li C, Fu CH, Guo YB, Fang FZ (2016) A multiscale modeling approach for fast prediction of part distortion in selective laser melting. J Mater Process Technol 229:703–712. https://doi.org/10.1016/j.jmatprotec.2015.10.022

[24] Chen Q, Liang X, Hayduke D, Liu JK, Cheng L, Oskin J, Whitmore R, To AC (2019) An inherent strain based multiscale modeling framework for simulating part-scale residual deformation for direct metal laser sintering. Addit Manuf 28:406–418. https://doi.org/10.1016/j.addma.2019.05.021

[25] Gh Ghanbari P, Mazza E, Hosseini E (2020) Adaptive local-global multiscale approach for thermal simulation of the selective laser melting process. Addit Manuf. https://doi.org/10.1016/j.addma.2020.101518

[26] Gu D, Shi X, Poprawe R, Bourell DL, Setchi R, Zhu J (2021) Material-structure-performance integrated laser-metal additive manufacturing. Science 372:6545. https://doi.org/10.1126/science.abg1487

[27] Wegst UG, Bai H, Saiz E, Tomsia AP, Ritchie RO (2015) Bioinspired structural materials. Nat Mater 14(1):23–36. https://doi.org/10.1038/nmat4089

[28] Cipriani CE, Ha T, Martinez Defilló OB, Myneni M, Wang Y, Benjamin CC, Wang J, Pentzer EB, Wei P (2021) Structure–processing–property relationships of 3D printed porous polymeric materials. ACS Mater Au 1(1):69–80. https://doi.org/10.1021/acsmaterialsau.1c00017

[29] Tamanna N, Crouch R, Naher S (2019) Progress in numerical simulation of the laser cladding process. Opt Lasers Eng 122:151–163. https://doi.org/10.1016/j.optlaseng.2019.05.026

[30] Jiang Q, Liu H, Li J, Yang D, Zhang Y, Yang W (2020) Atomic-level understanding of crystallization in the selective laser melting of Fe50Ni50 amorphous alloy. Addit Manuf. https://doi.org/10.1016/j.addma.2020.101369

[31] Zhang Y, Liu H, Mo J, Wang M, Chen Z, He Y, Yang W, Tang C (2019) Atomic-level crystallization in selective laser melting fabricated Zr-based metallic glasses. Phys Chem Chem Phys 21(23):12406–12413. https://doi.org/10.1039/c9cp02181g

[32] Li X, Guan Y (2020) Theoretical fundamentals of short pulse laser–metal interaction: a review. Nanotechnol Precision Eng 3(3):105–125. https://doi.org/10.1016/j.npe.2020.08.001

[33] Kaganov MI, Lifshits IM, Tanatarov LV (1957) Relaxation between electrons and the crystal lattice. Sovphysjetp

[34] Jones RE, Templeton JA, Wagner GJ, Olmsted D, Modine NA (2010) Electron transport enhanced molecular dynamics for metals and semi-metals. Int J Numer Methods Eng 83(8–9):940–967. https://doi.org/10.1002/nme.2857

[35] Thompson AP, Plimpton SJ, Mattson W (2009) General formulation of pressure and stress tensor for arbitrary many-body interaction potentials under periodic boundary conditions. J Chem Phys 131(15):154107. https://doi.org/10.1063/1.3245303

[36] Compute stress/atom command-LAMMPS document (2021). https://docs.lammps.org/compute_stress_atom.html.

[37] Hsiau SS (2000) Effective thermal conductivities of a single species and a binary mixture of granular materials. Int J Multiph Flow 26(1):83–97. https://doi.org/10.1016/S0301-9322(99)00003-8

[38] Mishra AK, Aggarwal A, Kumar A, Sinha N (2018) Identification of a suitable volumetric heat source for modelling of selective laser melting of Ti6Al4V powder using numerical and experimental validation approach. Int J Adv Manuf Technol 99(9–12):2257–2270. https://doi.org/10.1007/s00170-018-2631-4

[39] Zhang Y, Zhang J (2016) Sintering phenomena and mechanical strength of nickel based materials in direct metal laser sintering process—a molecular dynamics study. J Mater Res 31(15):2233–2243. https://doi.org/10.1557/jmr.2016.230

[40] Zhang Y, Wu L, El-Mounayri H, Brand K, Zhang J (2015) Molecular dynamics study of the strength of laser sintered iron nanoparticles. Proc Manuf 1:296–307. https://doi.org/10.1016/j.promfg.2015.09.031

[41] Meng L, Zhang Y, Yang X, Zhang J (2019) Atomistic modeling of resistivity evolution of copper nanoparticle in intense pulsed light sintering process. Physica B 554:31–34. https://doi.org/10.1016/j.physb.2018.11.036

[42] Zhang Y, Wu L, Guo X, Jung Y-G, Zhang J (2016) Molecular dynamics simulation of electrical resistivity in sintering process of nanoparticle silver inks. Comput Mater Sci 125:105–109. https://doi.org/10.1016/j.commatsci.2016.08.047

[43] Zhang Y, Liu H, Mo J, Wang M, Chen Z, He Y, Yang W, Tang C (2018) Atomic-scale structural evolution in selective laser melting of Cu50Zr50 metallic glass. Comput Mater Sci 150:62–69. https://doi.org/10.1016/j.commatsci.2018.03.072